Multi-scale flume investigation of the influence of cylindrical baffles on the mobility of landslide debris

Beom-Jun Kim

Research Professor (Ph. D.)

Institute for Disaster Prevention, Gangneung-Wonju National University,

Jukheon-gil 7, Gangneung-si 25457, South Korea,

Phone: +82-33-640-2419, E-mail: caper1004s@gwnu.ac.kr

Clarence Edward Choi

Assistant Professor (Ph. D.)

Department of Civil Engineering, The University of Hong Kong,

Pok Fu Lam, Hong Kong SAR, China,

Phone: +852-2589-1980, Fax: +852-2559-5337, E-mail: cechoi@hku.hk

ORCID number: 0000-0002-9712-1524

Chan-Young Yune (*corresponding author*)

Professor (Ph. D.)

Department of Civil Engineering, Gangneung-Wonju National University,

Jukheon-gil 7, Gangneung-si 25457, South Korea,

Phone: +82-33-640-2423, Fax: +82-33-646-1391, E-mail: yune@gwnu.ac.kr

ORCID number: 0000-0003-0477-2625

Abstract

Debris flows travel downslope at high speed and often cause damage to the infrastructure of societies around the world. With increasing extreme rainfall events and urbanization in mountainous regions, effective structural countermeasures are in increasing demand. Over recent years, engineers have proposed the installation of an array of cylindrical columns, called baffles, to reduce the velocity of debris flows in catchments. However, existing design methods are highly empirical in nature, so it is unclear whether they are adequate or over designed, and appropriate specifications and arrangement of cylindrical baffles have still not been suggested. Moreover, previous experimental studies have predominantly modeled debris flows as dry granular flows at a laboratory scale. In this study, to investigate the effect of cylindrical baffles on the dynamic characteristics of debris flow, a series of small-scale flume tests was conducted using a flume equipped with devices to measure the flow interaction between baffles and the dynamic loads of debris flow. In addition, to investigate the scale effect of debris flows and cylindrical baffles on flow characteristics, large-scale tests were also performed according to different numbers of rows of baffles for similar baffle configurations confirmed by small-scale tests. Using the small- and large-scale test results, this study analyzed the energy dissipation and dynamic impact characteristics according to the height and number of rows of baffles. The analysis results showed that the use of baffles increased the energy dissipation of debris flows, and an additional row of baffles produced greater effects on the energy dissipation in the debris flows. Based on the test results, the average dynamic pressure coefficient for cylindrical baffles was 0.31.

Keywords: Debris flow, Cylindrical baffle, Baffle height, Number of rows, Velocity, Dynamic load, Energy dissipation, Dynamic pressure coefficient

1. Introduction

Climate change has increased the frequency of extreme rainfall events, which has been reported to trigger more debris flows (Ren 2014; Stoffel et al. 2014). At the same time, urbanization in undeveloped mountainous areas is exposing humans to increased risk (Cui et al. 2019). If continuous development proceeds in mountainous regions, cost effective and robust structural countermeasures to mitigate the increasing threat posed by debris flows will be needed. Recently, among the variety of structural countermeasures available, there is also an increasing demand for compact and easy-to-install solutions that blend in well with the natural environment. In particular, baffles present a viable alternative to bulky and visually intrusive reinforced concrete barriers. An array of cylindrical or rectangular baffles is often constructed in the flowing path of debris flows, with the aim of perturbing the flow pattern of a debris flow to dissipate its flow kinetic energy. Fig. 1 shows cylindrical debris flow baffles installed at Lantau Island in Hong Kong, China. Despite the clear advantages of baffles, so far they have been designed empirically. This means that it is unclear whether their design is adequate or over designed. More importantly, design engineers have little to no guidance on what dimensions are required for individual baffles or how to space them relative to each other. Over recent years, there have been many experimental studies for modelling dry granular flows or debris flows that impact baffles. In particular, studies on the interaction between dry granular flows and arrays of mounds (Hákonardóttir 2004) or baffles (Choi 2013; Choi et al. 2014a; 2014b; Ng et al. 2014; Fei et al. 2020) have been carried out using small-scale physical experiments. These studies revealed several key interaction mechanisms, including dead zone development (Gray et al. 2003), run-up (Chu et al. 1995; Choi et al. 2015a) and overflow (Choi et al. 2016). Based on these observed mechanisms, optimal geometries were recommended for maximizing the energy dissipation of dry granular flows. Jóhannesson and Hákonardóttir (2003) recommended that the height of the mounds should be two to three times that of the upstream flow depth. The mounds should form steep upstream angles with the slope to enhance energy dissipation and be positioned closely together to allow the jets to deflect sideways to interact with each other and further dissipate energy. Finally, the aspect ratio of each mound should be unity and the slit opening between them should be as small as is deemed affordable. An optimized row of mounds can provide up to 20% energy dissipation. Hákonardóttir's work also revealed that successive rows of obstacles should be positioned to intercept overflow from the preceding row (Hákonardóttir 2004). Choi and Law (2015) recommended an optimum geometric configuration entailing baffle heights at least 1.5 times the upstream flow depth, with at least two staggered rows and an optimum row spacing of L/s = 3 (where L is the spacing between rows and s is the slit size between baffles). An optimized baffle configuration provided up to 50% of energy dissipation. Although dry granular flow within a scaled-down channel constitutes a highly-repeatable benchmark for investigating flow-structure interaction, scientific recommendations for designing debris flow baffles cannot be based on such results. This is partly because the fluid phase (i.e., water) is fundamentally neglected: dry granular flow cannot be assumed to behave like natural debris flow where the interstitial fluid vitally controls debris flow mobility (McArdell et al. 2007). Wang et al. (2017a; 2017b) conducted a series of small-scale experiments to study debris flows impacting an array of baffles. They proposed an optimum configuration of baffle arrays through the energy reduction of debris flow for various shapes and spacings of baffles. However, debris flow behavior is highly scale-dependent (Iverson 2015). More specifically, small-scale representations of debris flows may exhibit slight disproportionalities in terms of viscous shearing and pore pressures. The significance of these scale effects on debris flow-baffle interaction have yet to be evaluated. Evidently, existing recommended configurations from experimental studies are mutually inconsistent. Some studies were conducted using dry granular flows and some were conducted using two-phase flows. More importantly, the above studies were conducted at different scales. Thus, despite the large library of work conducted, there still lacks design guidelines rooted in science.

In this study, we adopted a multi-scale approach to reveal the optimum configuration of baffles. Small-scale flume tests were performed according to the various baffle heights and numbers of rows of installed baffles in the flume. High speed cameras and digital cameras to capture the flow interaction with baffles were installed at the top and side of the flume. A load cell for estimating the impact load of the debris flow was also installed behind the baffle. To investigate the scale effect of debris flows and cylindrical baffles on flow characteristics, large-scale tests were also conducted with baffle configurations similar to the small-scale tests. After the tests, the velocity, impact load, and energy dissipation due to baffle array conditions were analyzed. In addition, an appropriate dynamic pressure coefficient for the design of cylindrical baffles was suggested based on the results of small-scale and large-scale tests.

2. Methodology

2.1. Flume model

Fig. 2 shows a long rectangular flume with an overall length of 5.0 m, a side height of 0.45 m, and a base width of 0.3 m, designed for small-scale tests with baffles. The width of the flume was determined as a similarity ratio (1/17) to the valley of a watershed as in a real-scale experiment site in Korea (Jun et al. 2015). The flume, which was made of 10-mm thick acrylic plate, was reinforced with a stainless-steel frame. As shown in Fig. 2, the flume has a container for the storage of debris and water mixture at the upper end and a baffle zone for the installation of cylindrical column structures at the middle. The debris and water are stored at the storage container located at the uppermost upstream end of the flume and the container has an automatic spring-loaded system for opening/closing the door, which is secured with an electromagnetic lock. To capture the flow velocity of the free surface of debris flows and the flow interaction with the baffle array, high-speed cameras (HAU-U2) were installed at the top and side of the flume. The resolution of the high-speed camera is dependent on the speed: 500 frames per second with 800×600 pixels (top view) and 300 frames per second with 1024×768 pixels (side view). As shown in Fig. 3, we determined the diameter of the cylindrical baffles as 30 mm considering the similarity with the real baffles constructed at the real-scale experiment site (Jun et al. 2015). Baffles with various heights (40 and 80 mm) were manufactured to study the influence of baffle height on the debris flow behavior. To estimate the dynamic impact load of debris flows, as shown in Fig. 4, a load cell (Kyowa-LUX-B) was combined with the baffle horizontally. Fig. 5 shows an image of the small-scale test setup.

In this study, a large-scale test was also conducted using the large flume of Hong Kong University of Science and Technology (HKUST). Fig. 6 shows the test setup of the flume with a rectangular cross-sectional area. The whole length of the flume was 28.0 m with a base width of 2.0 m and a side height of 1.0 m to carry out the large-scale physical experiment. The width of the large-scale flume was about 7.0 times greater than the small-scale flume. The capacity of the storage container was 10 m^3 which is about 90 times greater than that of the small-scale flume. As shown in Fig. 6, the flume consists of three parts: a soil container, a transportation zone, and a deposition zone. The storage container occupies the first 5.0 m of the flume, which is inclined at 30°. The second part is 15.0 m in length and is inclined at 20°, which has a similar inclination of the transportation zone of debris flows that occurred in Korea (Jun et al. 2015). Then the horizontal deposition zone with a length of 8.0 m is extended to the end of the flume. The flume was made of reinforced acryl and steel frames were attached at the side of the flume to prevent deformation and to make the visual observation of the flow possible. The storage container with a double door system with water-tight sealings around its edges was used to retain debris material. To measure the upstream and downstream flow velocity during the test process, several lines were drawn at an interval of 1.0 m in the transverse direction at the bottom of the flume. To capture the flow kinematics of debris flows, the high-speed camera at the top of the flume and a digital camera at the side of the flume were installed. Moreover, we also used an unmanned aerial vehicle (UAV) in the air above the flume. The high-speed camera (model FR-Stream 4Coaxp Norpix) and the digital camera (GoPro) were installed and could capture images at 560 frames per second with a resolution of 2336 × 1728 pixels at 120 frames per second with 1280×720 pixels. The camera incorporated with the UAV (DJI Phantom 3 Professional), which had a resolution capability of 30 frames with 1280×720 pixels, could capture flow behavior in the air above the flume. Un-instrumented baffles and instrumented baffles with the impact load measurement of debris flow were made of stainless steel. As shown in Fig. 7, the non-instrumented baffle (Fig. 7(a)) was 219 mm in diameter, whereas the instrumented baffle (Fig. 7(b)) was 238 mm in diameter as the load cell was installed inside the baffle. The size of the cylindrical baffle was determined based on the ratio of the width between the large- and small-scale flumes (about 7.0 times). Fig. 8 shows an image of the large-scale test facility used in this study.

2.2. Scaling

For small- and large-scale experiments, the Froude number has been generally adopted to consider the scale effect of debris flows because debris flows are highly scale-dependent (Iverson, 2015). The Froude number is defined as the ratio of inertial force to the gravitational force, and is given as follows:

$$Fr = \frac{v}{\sqrt{ghcos\theta}} \qquad (1)$$

where v is the velocity $(\mathrm{m/s})$, h is the flow depth (m), g is the gravitational acceleration $(\mathrm{m/s^2})$, and θ is the slope angle (°).

The approaching Froude number ranged from 0.5 to 7.6 in previous studies (Arattano et al.

1997; Choi et al. 2015b; Cui et al. 2015; Hübl et al. 2009; Scheidl et al. 2013; Wang et al. 2018). For debris flows caused by heavy rainfall, however, a Froude number greater than 10 has been adopted in water-dominant debris flows for the simulation of rapid flow movement (Choi et al. 2017). In this study, to reproduce a debris flow with rapid flow characteristics caused by a typhoon and heavy rainfall, the approaching Froude number upstream of the baffles was determined as 8.0.

2.3. Test condition and procedure

In order to reproduce the debris flow behavior in the flume, a prototype flow was simulated as an ideal two-phase mixture of granular materials. For the small-scale test, the granular materials were made to be similar to the grain size distribution in the debris hazard site at Samcheock, Korea where a debris flow occurred in 2019. The debris mixtures were composed of 25% gravel (5-10 mm in diameter), 25% coarse sand (2-5 mm in diameter), and 50% medium to fine sand (0.25-2.0 mm in diameter). Fig. 9 shows a comparison of the grain size distribution for the mixed debris materials and the natural weathered soil collected from the debris hazard site in Samcheok, Korea. As shown in Fig. 9, two types of materials, gravel and sand, exhibited a similar grain size distribution. Since silt and clay size materials adhered to the side walls and made it impossible to analyze the moving particle images, to obtain a clear observation of the flow dynamics, they were excluded from the debris mixture. Instead, to reproduce the viscous flow characteristics of debris flows (granular-fluid mixtures), glycerin was mixed with the debris mixtures and water. The volumetric solid fraction of the debris flow tested was determined to be 50% and the dynamic viscosity of the debris specimen as about 0.05 pa·s, which was measured by a large vane rheometer test, was achieved. In addition, prior to the small-scale flume test with various baffle arrays, run-out tests for two types of debris materials with two rows of baffles was conducted. Dynamic similarity upstream between the reproduced two-phase soil mixture and the natural weathered soil of the debris hazard site was also confirmed as shown in Fig. 10 where the Froude number was measured at the 0.1 m upstream before the array of baffles. After the test, to simulate the dynamic similarity ($Fr =$ 8.0) of debris flows approaching upstream of the baffles, a series of preliminary tests under various flume inclinations with no baffles was conducted to consider the change in the total discharge of a debris flow as well. From this, we determined the flume inclination (29°) and the total mass of debris (20 kg) to carry out the small-scale flume test. With these test conditions, a predetermined Froude number scaling ($Fr \approx 8.0$) could be achieved with an approaching velocity of 3.3 m/s and a flow depth of 0.02 m.

To capture the dynamic loading for the baffle, a high sampling rate of 5 kHz from the load cell was selected. Fig. 11 shows the array of cylindrical baffles installed in two rows in the small-scale flume. To measure the dynamic impact load, the bottom of the cylindrical baffle with a load cell was detached from the flume and they were fixed by a rectangular column which was firmly fixed to the flume as shown in Fig. 12. The transverse blockage ratio, defined as the ratio of baffle width along the transverse direction to the flume width, was determined to be 40%, as proposed by Watanabe et al. (1980) and Ikeya and Uehara (1980). Once the baffles were installed, as shown in Fig. 2, high-speed cameras were installed at 0.1 m (upstream direction) and 1.4 m (downstream direction) upstream from the first row of baffles and downstream from the last row of baffles. During the flow process, the estimation of frontal velocity in all tests was based on captured image profiles using the high-speed cameras installed on side of the flume. Because the high-speed camera can capture images at 300 frames per second with a resolution of 1280 × 768 pixels, an accurate velocity estimation is possible through front flow movement and particle tracking in the images taken by the high-speed cameras. A digital camera was also installed at the side of the baffle array to observe the overall behavior of the debris flow dynamics along the flume at 240 frames per second with a resolution of 1920×1080 pixels. After all the cameras were installed, the granular-fluid mixtures were poured into the storage container at the top of the flume. At this stage, to prevent sedimentation of the prepared debris in the storage container, the mixtures were continuously stirred by an electric hand mixer. Then, the debris was discharged with the opening of the trap door. The initial bulk density and the initial volume in the storage container was 1,925 kg/m^3 and 0.015 m^3, respectively. After the test, the velocity and flow depth upstream and downstream were estimated by the captured image profiles through the high-speed camera. The estimated velocity based on the high-speed camera was verified by particle image velocimetry (PIV) analysis, and the velocity estimated by both methods was similar. The impact load was also estimated by the recorded loading data of a load cell.

In order to investigate the flow characteristics for an increased magnitude of debris flow and baffle arrays, large-scale flume tests were performed under the similar test conditions with the small-scale flume test. Because it is difficult to conduct a large number of tests at a large scale, the test conditions were determined based on the results of the small-scale flume test. In the large-scale flume tests, the height of the baffles was fixed as 304 mm and two and four rows of baffles were investigated. Considering the similarity ratio to the small-scale test (1/7), the height of baffles in the large-scale test corresponded to the case of the small-scale flume with 40 mm height baffles. Fig. 13 shows the array of cylindrical baffles in two rows in the large-scale flume. The cylindrical baffles were installed at the large flume, and the baffle at the center of each row had a load cell to measure the dynamic impact load with a sampling rate of 2 kHz. The transverse blockage ratio was about 44%, which was similar to the small-scale test. A high-speed camera and digital cameras were installed at the top and side of the flume to measure the velocity and flow depth. Subsequently, a two-phase debris flow was reproduced by mixing gravel, sand, clay, and water in the storage container. In this study, a representative debris mixture of East Asia was selected, and it had similar ranges with the debris mixtures of the debris hazard site in Korea (Ng et al. 2019). The debris mixture was composed of 36% gravel (20 mm in diameter), 61% sand (0.25-0.5 mm in diameter), and 3% silt (< 63 μm in diameter). The initial bulk density and the initial volume in the storage container were about 2,000 kg/m^3 and 3.0 m^3, respectively. The volumetric solid fraction of reproduced debris flow was 55%. The initial bulk density and the initial volumetric solid fraction of debris flow for each test was similar to each other. When the debris preparation and the camera installation were complete, the debris mixture was released from the storage container by opening of the trap door. During the test, the flow interactions upstream and downstream of the baffles were captured by the high-speed cameras and digital camera and the impact load was measured by the load cell. The test conditions are summarized in Table 1.

3. Small-scale test

3.1. Flow kinematics and velocity reduction

The kinematics of the flow flowing through the baffle arrays can be categorized as initial inflow, run-up, and overflow after impact. Fig. 14 shows a comparison between the observed kinematics captured by the high-speed camera and the analysis by particle image velocimetry (PIV) for test SH40_R2 from the side of the small-scale flume. In Fig. 14 (a) the flow front entered into the first row of baffles along the downslope direction. After the front flow impacted the first row of baffles, the run-up of the debris flow occurred almost perpendicular to the bottom of the flume while the rest of the debris flow was concentrated among the first row of baffles and the discharged front flow reached the second row of baffles. Here, the flow depth approaching the baffles increased as the effect of jet flow increased (Fig. 14 (b)). As the flow impacted the second row of baffles, the run-up occurred sequentially and the flow height around the second row of baffles was higher than the baffle height (Fig. 14 (c)). The image analysis revealed that the flow became dispersed as the front flow started to interact with the baffle. Subsequently, there was a flow velocity reduction due to consecutive impacts after the second row of baffles. As the inflow from upstream gradually increased, the upstream flow depth reached a maximum height, and the flow jets between the baffles of the first row consecutively continued to be deflected by the staggered arrays of the second row of baffles. Subsequently, overflow over the baffle arrays began to be observed (Fig. 14 (d)). Here, the flow depth increased up to 2.5 times than the baffle height of the second row. Fig. 15 shows the side view of the flow interacting with various numbers of rows of baffles. Observing the flow depth indicated as a dashed line in Fig. 15, we see that one row of baffles did not have a major effect on the flow impedance because the flow discharged between the baffles was not intercepted (Fig. 15 (a)). However, the increase in the number of rows of baffles from 2 to 4 exhibited an additional impedance of flow within the baffle array (Figs. 15 (b) and (c)) and, accordingly, the flow depth around the baffle arrays significantly increased.

Fig. 16 shows the change of frontal velocity along the transportation zone of the flume with various heights and numbers of rows of baffles. The distance traveled along the transportation zone for each test was normalized with the whole length of the flume ($L_w = 4.0$ m, including the length of the storage container). The frontal velocity was estimated from upstream (L/L_w= 0.36) to downstream (L/L_w= 0.86) of the baffle array. In the baffle zone, the frontal velocity was estimated sequentially at intervals of 0.2 m, which was the same distance as the spacing of baffle rows. For the estimation of frontal velocity in all tests, high speed images from the side view of the flume were used because the frontal velocity estimation based on the free surface above the flow was difficult due to the run-up and overflow of debris flows. All tests exhibited an increase in frontal velocity after being released from the storage container, and the velocity of the approaching flow reached about 3.3 m/s before entering the baffle arrays. Meanwhile, the frontal velocity after passing through the array of baffles showed a distinct change for each type of baffle configuration. For the case with no baffles (SH0), a continuous and gradual increase in frontal velocity was observed because of the absence of the interference of baffles. One row of baffles (SH40_R1 and SH80_R1) had a minor effect on the frontal velocity because 60% of the flow (40% of blockage ratio) freely passed between the baffles without any interference, as observed in previous researches (Ng et al. 2014). However, with two and four rows of baffles (SH40_R2, R4 and SH80_R2, R4), a rapid decrease in velocity was observed until the final row of baffles, even though the decreasing ratio decreased after the second row of baffles. Two rows of baffles (SH40_R2) exhibited a 22% frontal velocity reduction at L/L_w= 0.59 compared with the case of no baffle, after which the frontal velocity at L/L_w= 0.71 increased by 15%, which was similar to the case without baffles. The addition of baffle rows (SH40_R4) led to an additional 23% of frontal velocity reduction at L/L_w= 0.71 compared with two rows of baffles (SH40_R2). Furthermore, installing taller baffles in two rows (SH80_R2) exhibited a 33% frontal velocity reduction at L/L_w= 0.71 compared with the case with shorter baffles (SH40_R2). By increasing the number of rows of taller baffles from 2 (SH80_R2) to 4 (SH80_R4), the frontal velocity at L/L_w= 0.71 after passing through the array of baffles decreased by up to 41%. Taller baffles produced a higher impedance of flow, but increasing the number of rows provided greater energy dissipation in the baffle arrays. In Fig. 16, an increase in the frontal velocity downstream after passing through the array of baffles was observed for all cases due to a gradual acceleration of debris flow by the transportation process in the remaining part of the flume.

3.2. Impact load characteristics

Fig. 17 shows a comparison of impact load versus time for various baffle heights. To investigate the overall impact load behavior against debris flow, the impact load was measured in the baffle array with four rows of baffles. During flow process, the starting time of impact at the first row was set to t = 2.0 s, and the total testing time was about 5.0 s. The largest impact load for each row of baffle is also indicated in the figure (first, second, third, and fourth row). For short baffles (SH40), comparing the time histories for the peak impact of each baffle, the peak impact load for the first row of baffles was at t = 0.02 s. The peak impact load at the second, third, and fourth rows of baffles was at t = 0.14, 0.22, and 0.34 s, respectively. After the impact load reached the peak value, it did not remain in a static state but decreased quickly as the flow discharged downstream. During the impact process, the highest peak impact load occurred at the second row of baffles, and it was 36% higher than that measured at the first row of baffles. This was because the jet flow, which discharged from openings of the first row of baffles, impacted the second row of baffles with increased flow depth. The increased flow depth induced the increase of impacting area in the second row of baffles. As shown in Fig. 16, the flow velocity decreased slightly after the first row of baffles and then decreased significantly after the second row of baffles. Therefore, the effect of increased impacting area was more dominant than the decreased frontal velocity at the impact against the second row of baffles. After the second row of baffles, however, the impact load decreased up to an average of 28% compared with the impact load at the first row of baffles as the flow was continuously intercepted by the additional staggered rows. For tall baffles (SH80), the peak impact at the first, second, and third rows of baffles were at t = 0.03, 0.24, and 0.25 s, respectively, which was a 37% longer time on average compared with the case with short baffles (SH40). The impact load at the fourth row of baffles could not be measured due to a problem in the load cell. The reason for the longer time for the peak impact load in tall baffles was that the tall baffles had a higher impedance of flow than short baffles. The highest impact load was also measured at the second row of baffles and it was 55% higher than that measured at the first row of baffles. The impact load at the third row of baffles, then, began to decrease with the continuous interception of flow from the second rows of baffles. Furthermore, because of the increased cross-sectional area of the taller baffles, there was a 43% increase in the peak impact load of second row of baffles compared with shorter baffles as it induced a higher flow impedance of baffles. However, shorter baffles caused a significant overflow over the second row of baffles, which generated a lower impact load than that of taller baffles. As already discussed for Fig. 16, the larger dynamic impact load in taller baffles produced a greater downstream velocity reduction than in shorter baffles. The frontal flow velocity before the first and second row of baffles was similar with each other, but the frontal velocity of taller baffles decreased much before the third row of baffles. Thus, the impact load at the first and second row of taller baffles were higher than that of the shorter baffles because of higher flow impedance by taller baffles. Therefore, not only increasing the number of rows of baffles but also increasing the baffle height can substantially contribute to the dissipation of potential downstream flow energy.

4. Experimental verification through large-scale test

4.1. Energy dissipation by baffle arrays

Fig. 18 shows a comparison of downstream velocity change for the small- and large-scale tests. The upstream and downstream frontal velocities, which was measured at a position with a similar scaling ratio for small- and large-scale tests, were used to estimate the velocity change ratio. In the figure, the velocity change ratio, defined as $((V_{upstream} - V_{downstream})/V_{upstream}) \times 100$, higher than 0 and lower than 0 represents the velocity increase and decrease downstream, respectively. For the small-scale test, the velocity slightly increased downstream by about 11 to 13% compared to the upstream velocity when there was no baffle or only one row of baffles. On the other hand, the velocity decreased downstream by about 14% and 33% for the two and four rows of baffles with a height of 40 mm (SH40_R2, SH40_R4), respectively. And the velocity downstream decreased further by about 39% and 65% for the two and four rows of baffles, respectively, with an increasing baffle height from 40 to 80 mm. Fig. 19 shows the kinematics of debris flow through two rows of baffles, as captured form the side of the large flume. The flow front rapidly entered into the upstream of the baffles (Fig. 19 (a)). The flow was consecutively affected by the first and second rows of baffles, and the run-up was observed behind the first row of baffles. After that, the dispersion of the flow due to continuous impacts of flow was observed around the array of baffles, and the overflow began to occur over the baffles (Fig. 19 (b)). As the flow jet was deflected by the staggered arrays of the second row of baffles, the effect of flow impedance increased, and then the flow depth increased up to 3.8 times than the baffle height of the installed second row (Fig. 19 (c)). The mutual interaction between the flow and the baffles for the large-scale test was similar to that of the small-scale test in Fig. 14.

For the large-scale test with two rows of baffles, the downstream velocity decreased by an average of 34% compared to the upstream velocity. Similar to the small-scale test, increasing the number of rows of baffles from 2 (L_R2) to 4 (L_R4) created a 32% further velocity reduction downstream. The frontal velocity and velocity change ratio for both upstream and downstream for all tests are summarized in Table 2. Although the frontal velocity both upstream and downstream of the large-scale test was about 2.0 times higher than that of the small-scale test, the tendency of the velocity reduction was similar. It is obvious that increasing the number of rows of baffles provides greater flow interference passing through the baffle arrays. Therefore, increasing the number of baffle arrays decreases the downstream discharge, and consequently the downstream flow energy is reduced.

The energy loss for various baffle arrays can be deduced by the law of conservation of energy (Choi et al. 2014a; Wang et al. 2017b; Kim 2021). Based on the difference in velocity, flow depth, and potential head upstream $(h_u + v_u^2/2g + z_u)$ and downstream $(h_d + v_d^2/2g + z_d)$, the energy loss ($E_u - E_d = \Delta E$) during the flow process for each test can be estimated. Here, E_u is the upstream flow energy; E_d is the downstream flow energy; and ΔE is the energy difference between the upstream and downstream baffle arrays. For simplicity, the flow was assumed to be incompressible so that the flow density did not change significantly during the test. Fig. 20 shows the comparison of the energy loss ratio ($\Delta E/E_a$) between upstream and downstream of the small-scale test and the large-scale test. The energy loss (ΔE) for each test was normalized by the approaching flow energy (E_a) right before the baffles. The results revealed that the use of baffle arrays increased the energy loss for both the small-scale and the large-scale tests. For the small-scale test, the energy loss for the cases with two rows of baffles increased by 35% as the baffle height increased from 40 to 80 mm. Taller baffles contributed to an increase of energy loss due to a higher impedance compared to shorter baffles. Moreover, additional numbers of rows of baffles can create greater energy loss of the baffle arrays. Increasing the number of rows of baffles from 2 rows (SH40_R2 and SH80_R2) to 4 rows (SH40_R4 and SH80_R4) provided an additional 21% of energy loss on average. However, an insufficient number of rows of baffles showed only a minor effect on the energy loss regardless of the baffle height. One row of baffles (SH40_R1 and SH80_R1) exhibited low energy loss similar to the case with no baffles (SH0). This was because the jet flow between baffles discharged without any interference. To induce an effective dissipation of flow energy, two or more rows of baffle arrays are needed regardless of baffle height. Likewise, increasing the number of rows of baffles in the large-scale test produced an additional energy loss of 20%. Fig. 21 shows a comparison of the energy loss for various baffle configurations for the small-scale test (ST) and the large-scale test (LT). In addition, in order to verify the energy loss in cylindrical baffles, the results of the energy loss for granular flows with various types of baffles from previous studies (Choi et al., 2014a; Kim, 2021) were added to the figure, and the trend lines for each test are plotted for reference. The solid line and the dashed line indicate the trend line for a granular flow and a two phase flow, respectively. The energy losses for the granular flow showed a linearly increasing trend as the number of rows of baffles increased regardless of baffle shape. In contrast, the energy loss for debris flows exhibited an abrupt increase when the number of rows of baffles increased from one to two both for small- and large-scale tests. Thus, the effect of an additional row of baffles is crucial, especially for two phase flows such as debris flows. Additional numbers of rows further perturbed the flow pattern and led to greater deflection of energy dissipation within the baffle arrays, and consequently, additional rows of baffles promoted the deflection of flow discharge, which led to more effective energy dissipation.

4.2. Normalized impact load

Fig. 22 shows the comparison of impact load versus time for four rows of baffles in the large-scale test. The impact load for the third row of baffles was not included in the figure because the impact load was not measured due to a problem with the load cell during the test process. The total testing time was 12.0 s. As the debris flow was impeded by baffles, a sharp increase of impact load was observed. After the initial impact of the debris flow, the flow reached the highest peak impact load. The peak loads of the first, second, and fourth rows of baffles were at t = 1.75, 2.15, and 3.60 s. Then, the impact load gradually decreased as the flow discharged downstream, and the impact process did not reach a static state until the end of the flow. In the baffle arrays, the impact load was sequentially recorded in the order of the first, second, and fourth row of baffles. The time histories for the impact load of the baffles were similar to the results of the small-scale test.

Fig. 23 shows the comparison of the peak impact load for four rows of baffles in the small-scale test (ST) and the large-scale test (LT). The impact load for each row of baffles was normalized with the impact load measured at the first row of baffles (L_{1st}). The results showed that the overall trend of the impact load exhibited a gradual reduction as the flow passed through the baffles. The highest peak impact load, however, was measured at the second row of baffles in the small-scale test while, in the large-scale test, it was measured at the first row of baffles. The peak impact load for the small-scale test at the second row of baffles was due to an increased jet flow after the first row of baffles (Fig. 14 (b) and (c)), and this impact load became higher as the baffle height increased. But, the peak impact load for the large-scale test occurred at the first row of baffles. Because of a higher depth of approaching flow upstream, a highest peak impact load occurred at the first row of baffles. Moreover, the jet flow after the first row of baffles had a higher flow depth than the baffle height, but the flow depth caused a significant overflow over the second row of baffles, which produced a lower impact load. Nevertheless, the impact load continuously decreased to the final row of baffles, and the reduction ratio of the impact load for the final row of baffles for both the small- and large-scale test was on average of 50% compared with the first row of baffles. Since the dynamic pressure is proportional to the density and the square of the flow velocity, the velocity reduction contributed most to the decrease of the impact load. Accordingly, the consecutive velocity reduction caused by the increased number of rows of baffles will be effective not only in energy dissipation but also in lessening the impact load.

4.3. Dynamic pressure coefficient

The debris flow impact load is one of the important parameters for designing hazard mitigation measures (Song et al. 2019), and is simultaneously the key aspect to guarantee the efficiency of baffle structure against debris flow. In current engineering practice, the dynamic impact load against debris flow countermeasures is estimated using the dynamic pressure coefficient. Generally, a dynamic pressure coefficient (α) higher than 1.0 has been recommended for the design of debris flow-resisting structures (Song et al. 2019; Kwan 2012).

For closed-type rigid barriers and flexible barriers, α = 2.5 (Kwan 2012) and α = 2.0 (Kwan and Cheung 2012) are used, respectively. In this study, dynamic pressure coefficients for cylindrical baffles were estimated based on the highest peak impact load, the frontal velocity, and the flow depth, which was measured at the first row of baffles for the small-scale test and the large-scale test. Eq. (2) represents the hydrodynamic approach model to estimate the impact load of debris flows. In this model, the flow is assumed to be incompressible so that the flow density does not change without reduction of the total mass because it is usually difficult to obtain an accurate flow density during the flow impact.

$$F = PA = a\rho v^2 hw \tag{2}$$

where α is the dynamic pressure coefficient, ρ is the bulk density of flow ($\mathrm{kg/m^3}$), v is the flow velocity ($\mathrm{m/s}$), h is the flow depth (m), and w is the flow width (m). Table 3 summarizes the Froude number, peak impact load, and dynamic pressure coefficient estimated from the small- and large-scale tests. To compare the dynamic flow characteristics for both the two tests, the Froude number and dynamic pressure coefficient of the small- and large-scale tests were estimated using the peak impact load for the first row of baffles and the frontal velocity approaching the upstream of baffle captured at the top of the flume. Although the highest peak impact load occurred at the second row of baffles, the flow parameters behind the first row of baffles were used to estimate the dynamic pressure coefficient. This was because the flow after passing through first row of baffles forms a jet flow, and then the density may be changed during the interaction between the flow and the baffles. This effect can lead to the uncertainty in term of dynamic pressure coefficient for design of baffles. By increasing the magnitude and size of the debris flow and baffles with the flume, the peak impact load of the large-scale test was 34 times higher than the impact load of the small-scale test, whereas the deduced dynamic pressure coefficients for the two tests were similar. Based on these tests, an average value of dynamic pressure coefficient was 0.31.

The deduced dynamic pressure coefficient (α) for the experimental tests were within a narrow range, and thus a comparison of values in a wide range can serve to bear additional insight on the relevance of the test results. Fig. 24 shows the relationships between the empirical dynamic pressure coefficient and the Froude number (N_{Fr}) from previous research, including this study, and the values were calculated by the dynamic impact at the front of baffles without the static impact by the flow. The estimated values were from the experimental or field monitoring results of previous studies (Proske et al. 2011; Hübl and Holzinger 2003; Zhang and Yuan 1985; Cui et al. 2015; Ng et al. 2016; Hu et al. 2020; Cho et al. 2020). In this figure, the empirical dynamic pressure coefficient exhibited substantial changes depending on the flow characteristics described as the Froude number. The dynamic pressure coefficient of cylindrical baffles in the study was consistent with previous research. In comparison to that discussed for energy loss and impact load characteristic (Figs. 19 and 22), the small-scale test and the large-scale test were different in the scale of debris flow and baffles, but the energy loss and impact load characteristics for the two tests showed a similar tendency. The results of the small-scale test can be used to determine further appropriate specifications and arrangements for baffle design. However, in an actual watershed, because of gravel and boulders with large size and high rigidity, we must keep in mind that the actual debris flow could have a higher impact load. Therefore, we need additional study for impact load considering the interaction between flows with large boulders and the structure.

5. Conclusions

In this study, to examine the energy dissipation and dynamic impact load of debris flow on cylindrical baffles, small-scale flume tests were conducted according to various baffle configurations. Moreover, to verify the experiment results for the scale effect of debris flow and cylindrical baffles on flow characteristics, large-scale tests were carried out as well. The results confirmed that the use of baffles reduced the frontal velocity and flow energy of debris flows, and it was effective in impeding flow mobility. Furthermore, increasing the number of rows of baffles increased the flow impedance due to the sequential cross-sectional obstruction in the flume and provided greater downstream energy loss. However, one row of baffles did not have a major effect on the energy dissipation. By increasing the scale of debris flow and baffles in the flume, the velocity and the impact load in the large-scale test were higher than the small-scale test, but the overall trend for both the energy loss and the impact load characteristics were similar. Based on the test results, the average dynamic pressure coefficient for cylindrical baffles was 0.31. For field application of baffles, however, additional study will be needed to investigate the effect of impact load with flow interaction including large boulders on the structure.

Acknowledgement

Funding: This research was supported by Basic Science Research Program through the National Research Foundation of Korea (NRF) funded by the Ministry of Education (2021R1A6A1A03044326).

References

Arattano, M., Deganutti, A.M., Marchi, L., 1997. Debris flow monitoring activities in an instrumented watershed on the Italian Alps. In: Proceedings of the 1st ASCE International Conference on Debris-Flow Hazards Mitigation: Mechanics, Prediction & Assessment. San Francisco, California, US, 7–9 August 1997. American Society of Civil Engineers, New York, pp. 506–515.

Choi, C.E., 2013. Flume and discrete element investigation of granular flow mechanisms and interaction with baffles. PhD Dissertation, The Hong Kong University of Science and Technology, Hong Kong, China.

Choi, C.E., Au-Yeung, S.C.H., Ng, C.W.W., Song, D., 2015a. Flume investigation of landslide granular debris and water runup mechanisms. Géotechnique Letters 5, 28-32. http://dx.doi.org/10.1680/geolett.14.00080.

Cui, Y., Cheng, D., Choi, C.E., Jin, W., Lei, Y., Kargel, J.S., 2019. The cost of rapid and haphazard urbanization: lessons learned from the Freetown landslide disaster. Landslide 16 (2), 1167-1176. https://doi.org/10.1007/s10346-019-01167-x.

Choi, C.E., Goodwin, G.R., Ng, C.W.W., Cheung, D.K.H., Kwan, J.S.H., Pun, W.K., 2016. Coarse granular flow interaction with slit structures. Géotechnique Letters 6, 267-274. https:// dx.doi.org/10.1680/jgele.16.00103.

Chu, T., Hill, G., McClung, D.M., Ngun, R., Sherkat, R., 1995. Experiments on granular flows to predict avalanche runup. Can. Geotech. J. 32 (2), 285–295. https://doi.org/10.1139/t95-030.

Cho, H.S., Kim, B.J., Yune, C.Y., 2020. Experimental study on the effect of arrangement of cylindrical countermeasures on debris flow impact load. J. Kor. Geotech. Soci. 36 (11), 135–148 (in Korean). https://doi.org/10.7843/kgs.2020.36.11.135.

Choi, C.E., Law, R.P.H., 2015. Performance of landslide debris-resisting baffles. HKIE Transactions 22 (4), 235-246. http://dx.doi.org/10.1080/1023697X.2015.1102658.

Choi, S.K., Lee, J.M., Kwon, T.H., 2017. Effect of slit-type barrier on characteristics of water dominant debris flow: small-scale physical modeling. Landslides 15 (1), 111–122. https://doi.org/10.1007/s10346-017-0853-4.

Choi, C.E., Ng, C.W.W., Au-Yeung, S.C.H., Goodwin, G.R., 2015b. Froude characteristics of both dense granular and water flows in flume modelling. Landslides 12 (6), 1197–1206. https://doi.org/10.1007/s10346-015-0628-8.

Choi, C.E., Ng, C.W.W., Law, R.P.H., Song, D., Kwan, J.S.H., Ho, K.K.S., 2014b. Computational investigation of baffle configuration on impedance of channelized debris flow. Can. Geotech. J. 52 (2), 182-197. https://doi.org/10.1139/cgj-2013-0157.

Choi, C.E., Ng, C.W.W., Song, D., Kwan, J.S.H., Shiu, H.Y.K., Ho, K.K.S., Koo, R.C.H., 2014a. Flume investigation of landslide debris-resisting baffles. Can. Geotech. J. 51 (5), 540–553. https://doi.org/10.1139/cgj-2013-0115.

Cui, P., Zeng, C., Lei, Y., 2015. Experimental analysis on the impact force of viscous debris flow. Earth Surf. Process. Landf. 40, 1644–1655. https://doi.org/10.1002/esp.3744.

Fei, J., Jie, Y., Sun, X., Chen, X., 2020. Experimental investigation on granular flow past baffle piles and numerical simulation using a μ(I)-rheology-based approach. Pow. Tech. 359, 36–46. https://doi.org/10.1016/j.powtec.2019.09.069.

Gray, J.M.N.T., Tai, Y.C., Noelle, S., 2003. Shock waves, dead zones and particle-free regions in rapid granular free-surface flows. J. Fluid Mech. 491, 161-181. https://doi.org/10.1017/ S00 22112003005317.

Hákonardóttir, K.M., 2004. The Interaction between snow avalanches and dams. PhD Dissertation, University of Bristol, England.

Hübl, J., Holzinger, G., 2003. Development of design basis for crest open structures for debris flow management in torrents: miniaturized tests for the efficiency estimation of debris flow breakers, WLS Report.

Hübl, J., Suda, J., Proske, D., Kaitna, R., Scheidl, C., 2009. Debris flow impact estimation steep slopes. In: Proceedings of the 11th International Symposium on Water Management and Hydraulic Engineering, Ohrid, Macedonia, pp. 1–4.

Hu, H., Zhou, G.G.D., Song, D., Cui, K.F.E., Huang, Y., Choi, C.E., Chen, H., 2020. Effect of slit size on the impact load against debris flow mitigation dams. Eng. Geol. 274 (5), https://doi.org/10.1016/j.enggeo.2020.105764.

Iverson, R.M., 2015. Scaling and design of landslide and debris-flow experiments. Geomorphology 244, 9–20. https://doi.org/10.1016/j.geomorph.2015.02.033.

Ikeya, H., Uehara, S., 1980. Experimental study about the sediment control of slit sabo dams. J. Jpn. Eros. Con. Eng. Soc. 114, 37–44 (in Japanese). https://doi.org/10.11475/sabo1973.32.37.

Jóhannesson, T., Hákonardóttir, K. M., 2003. Remarks on the design of avalanche braking mounds based on experiments in 3, 6, 9 and 34 m long chutes, Report 03024, IMO, Reykjavík.

Jun, K.J., Lee, S.D., Kim, G.H., Lee, S.W., Yune, C.Y., 2015. Verification of countermeasures by velocity estimation of real scale debris flow test. In: Proceedings of the 6th International Conference on Debris flow Hazard Mitigation: Mechanics, Prediction and Assessment (DFHM6), Tsukuba, Japan, 22–25 June 2015.

Kim, B.J., 2021. Experimental and numerical study on effect of cylindrical baffles on debris flow behavior. PhD Dissertation, Gangneung-Wonju National University, Korea (in Korean).

Kwan, J.S.H., 2012. Supplementary technical guidance on design of rigid debris-resisting barriers. In: GEO Report No. 270. Geotechnical Engineering Office, HKSAR Government.

Kwan, J.S.H., Cheung, R.W.M., 2012. Suggestion on design approaches for flexible debris-resisting barriers. In: Discussion note DN1/2012. Geotechnical Engineering Office, HKSAR Government.

McArdell, B.W., Bartelt, P., Kowalski, J., 2007. Field observations of basal forces and fluid pore pressure of debris flow. Geophys. Res. Lett. 340 (7), L07406. https://doi.org/10.1029/2006GL029183.

Ng, C.W.W., Choi, C.E., Song, D., Kwan, J.S.H., Shiu, H.Y.K., Ho, K.K.S., Koo, R.C.H., 2014. Physical modelling of baffles influence on landslide debris mobility. Landslides 12 (1), 1–18. https://doi.org/10.1007/S10346-015-0574-5.

Ng, C.W.W., Choi, C.E., Majeed, U., Poudyal, S., De Silva, W.A.R.K., 2019. Fundamental framework to design multiple rigid barriers for resisting debris flows. In: Proceedings of the 16th Asian Regional Conference on Soil Mechanics and Geotechnical Engineering, Taipei, Taiwan, 14–18 October 2019.

Ng, C.W.W., Song, D., Choi, C.E., Liu, L.H.D., Kwan, J.S.H., Koo, R.C.H., Pun, W.K., 2016. Impact mechanisms of granular and viscous flows on rigid and flexible barriers. Can. Geotech. J. 54 (2), https://doi.org/10.1139/cgj-2016-0128.

Proske, D., Suda, J., Hübl, J., 2011. Debris flow impact estimation for breakers. Georisk 40 (2), 143-155. https://doi.org/ 10.1080/17499518.2010.516227.

Ren, D., 2014. The devastating Zhouqu storm-triggered debris flow of August 2010: Likely causes and possible trends in a future warming climate. Geophys. Res. Atmos. 119 (7), 3643-3662. https://doi:10.1002/2013JD020881.

Scheidl, C., Chiari, M., Kaitna, R., Müllegger, M., Krawtschuk, A., Zimmermann, T., Proske, D., 2013. Analysing debris-flow impact models, based on a small-scale modelling approach. Surv. Geophys. 34 (1), 121–140. https://doi.org/10.1007/s10712-012-9199-6.

Song, D., Choi, C.E., Ng, C.W.W., Zhou, G.G.D., Kwan, J.S.H., Sze., H.Y., Zheng, Y., 2019. Load-attenuation mechanisms of flexible barrier subjected to bouldery debris flow impact. Landslides 16 (10), 2321-2334. https://doi.org/10.1007/s10346-019-01243-2.

Stoffel, M., Mendlik, T., Sshneuwly-Bollschweiler, M., Gobiet, A., 2019. Possible impacts of climate change on debris-flow activity in the Swiss Alps. Climatic Change. 122, 141-155. https://doi.org/10.1007/s10584-013-0993-z.

Wang, F., Chen, J., Chen, X., 2017a. Experimental study on the energy dissipation characteristics of debris flow deceleration baffles. J. Mt. Sci. 14 (10), 1951–1960. https://doi.org/10.1007/s11629-016-3868-8.

Wang, F., Chen, X., Chen, J., You, Y., 2017b. Experimental study on a debris-flow drainage flume with different types of energy dissipation baffles. Eng. Geol. 220, 43–51. https://doi.org/10.1016/j.enggeo.2017.01.014.

Wang, Y., Liu, X., Yao, C., Li, Y., Liu, S., Zhang, X., 2018. Finite release of debris flows around round and square piers. J. Hydraul. Eng. 144 (12). https://doi.org/10.1061/(ASCE)HY.1943-7900.0001542.

Watanabe, M., Mizuyama, T., Uehara, S., 1980. Review of debris flow countermeasure facilities. J. Jpn. Eros. Con. Eng. Society. 115, 40–45 (in Japanese). https://doi.org/10.13101/ijece.1.38.

Zhang, S., Yuan, J., 1985. Impact force of debris flow and its detection. In: Memoirs of Lanzhou Institute of Glaciology and Cryopedology, Chinese Academy of Sciences. Science Press, Beijing, pp. 269-274.

Table 1 The test conditions.

Baffle condition		Baffle height (H)	Number of rows (R)	Spacing between successive rows (L)	Blockage ratio (B)	Amount of soil	Designation
Small-scale test	Without baffles	-	—	—	—	20 kg	SH0
	With baffles	40 mm	1	-	40%		SH40_R1
			2	200 mm			SH40_R2
			4				SH40_R4
		80 mm	1				SH80_R1
			2				SH80_R2
			4				SH80_R4
Large-scale test	With baffles	304 mm	2	1.5 m	44%	11,484 kg	L_R2
			4				L_R4

Table 2 Comparison of flow velocity for all tests.

Test ID		Upstream, v (m/s)	Downstream, v (m/s)	Ratio
Small-scale test	SH0	3.30	3.73	+13%
	SH40_R1		3.65	+11%
	SH40_R2		2.85	-14%
	SH40_R4		2.20	-33%
	SH80_R1		3.70	+12%
	SH80_R2		1.92	-39%
	SH80_R4		1.14	-65%
Large-scale test	L_R2	6.66	4.42	-34%
	L_R4		2.99	-55%

Ratio: velocity increase [+], velocity decrease [-]

Table 3 Comparison of dynamic flow characteristics for each flume test.

Test ID		Density (kg/m^3)	Froude number (N_{Fr})	Peak impact load (N)	Dynamic pressure coefficient (α)
Small-scale test	SH40_R4	1,925	8.58	7.82	0.33
	SH80_R4		8.91	9.78	0.39
Large-scale test	L_R4	2,000	7.14	300.00	0.21

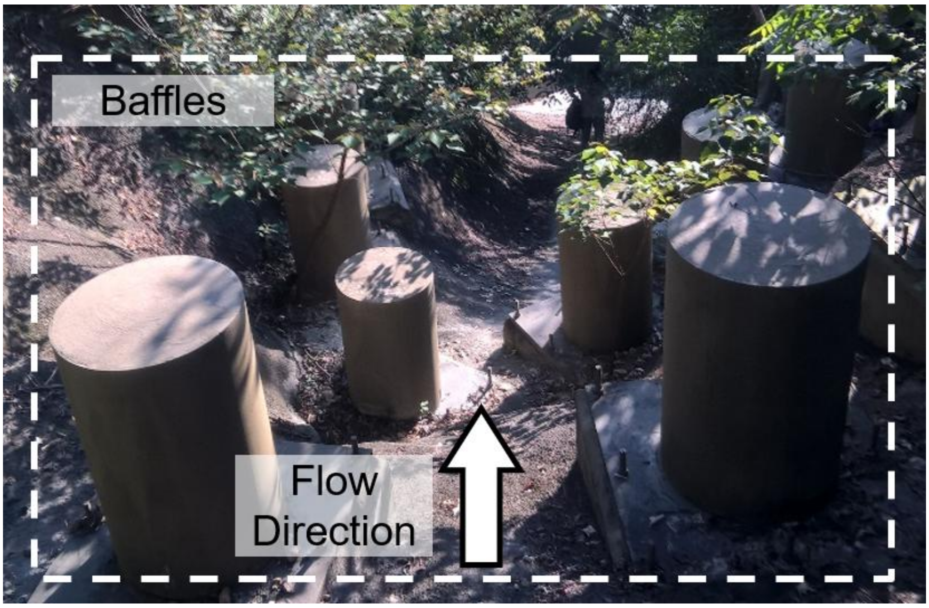

Fig. 1. Debris flow baffles installed at Lantau Island in Hong Kong, China.

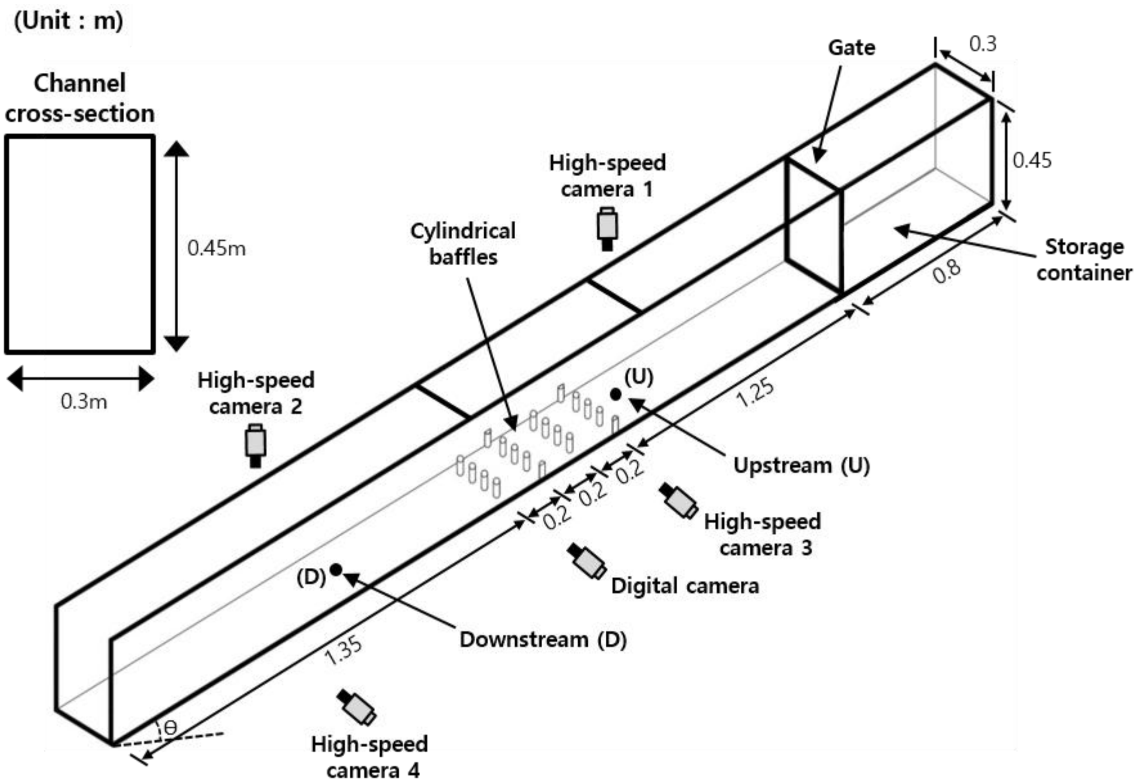

Fig. 2. Schematic diagram of the small-scale flume model.

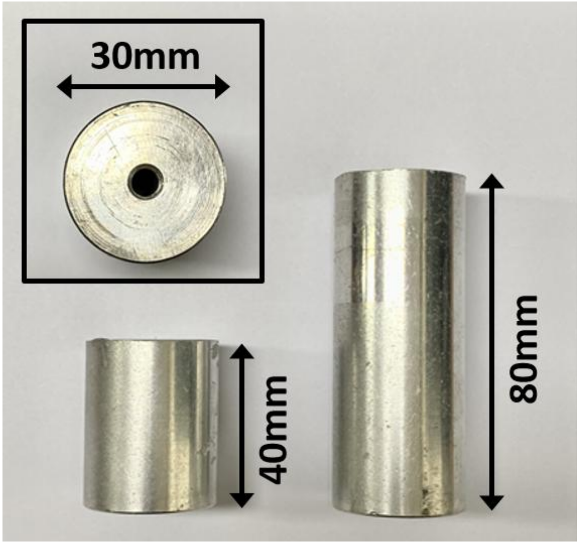

Fig. 3. Dimensions of the cylindrical baffles used in the experiment.

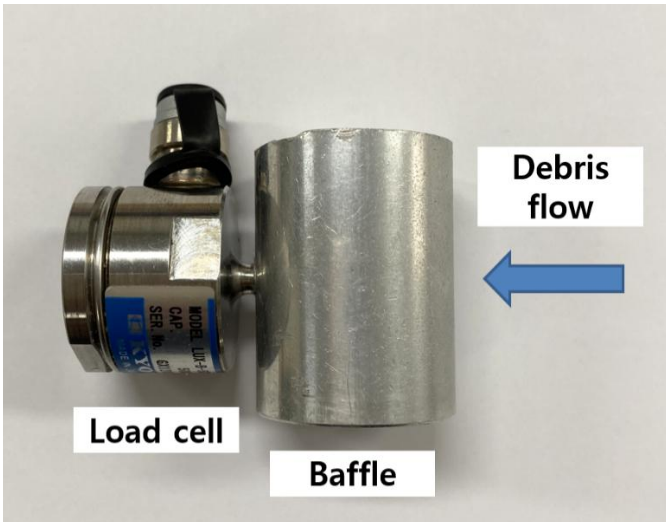

Fig. 4. Cylindrical baffle with a load cell.

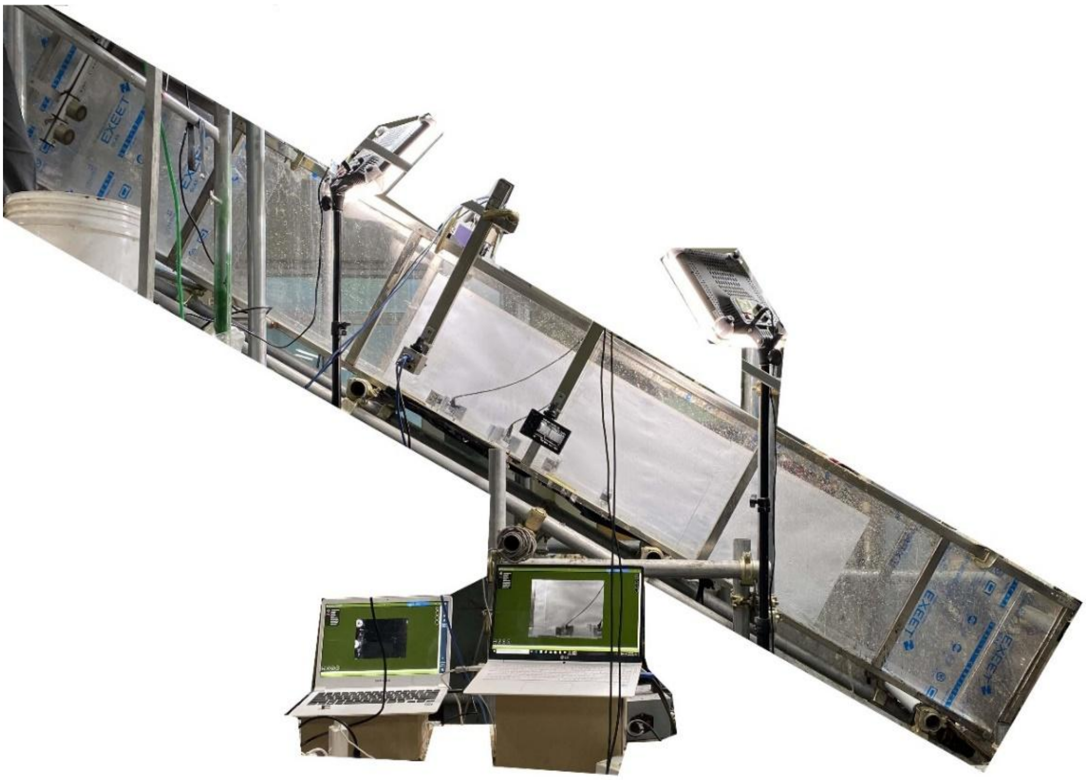

Fig. 5. Small-scale test setup.

Fig. 6. Plan view of a large-scale flume model (Kadoorie centre, Hong Kong, China).

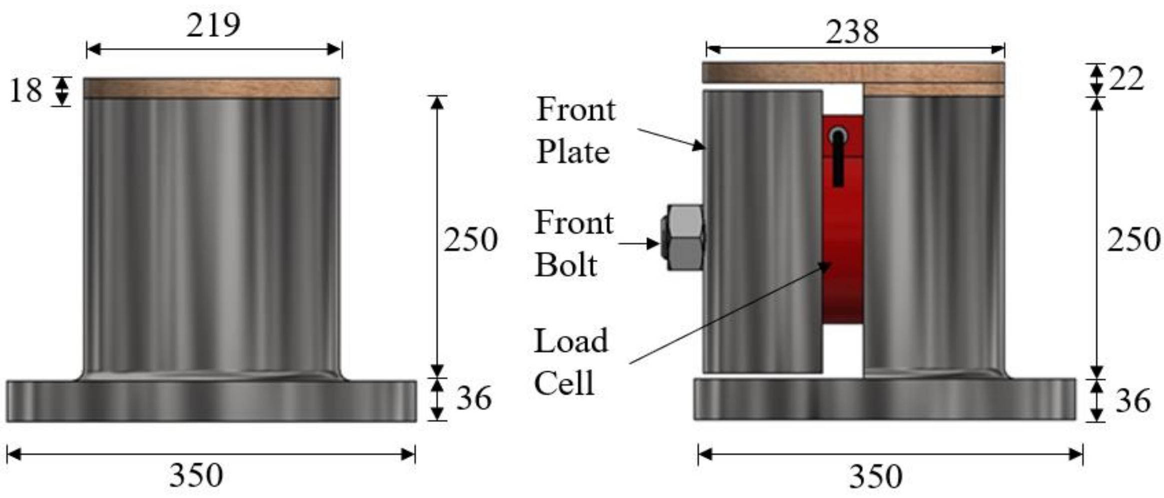

Fig. 7. Installation of cylindrical baffles in the large-scale test device: (a) un-instrumented baffle; (b) instrumented baffle.

Fig. 8. Large-scale test facility (Kadoorie centre, Hong Kong, China).

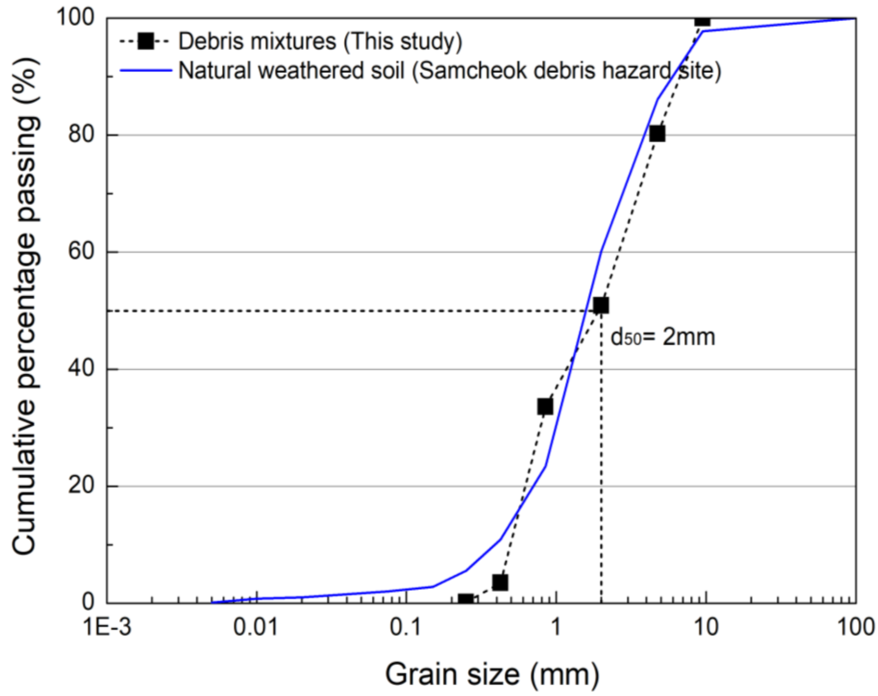

Fig. 9. Grain size distribution.

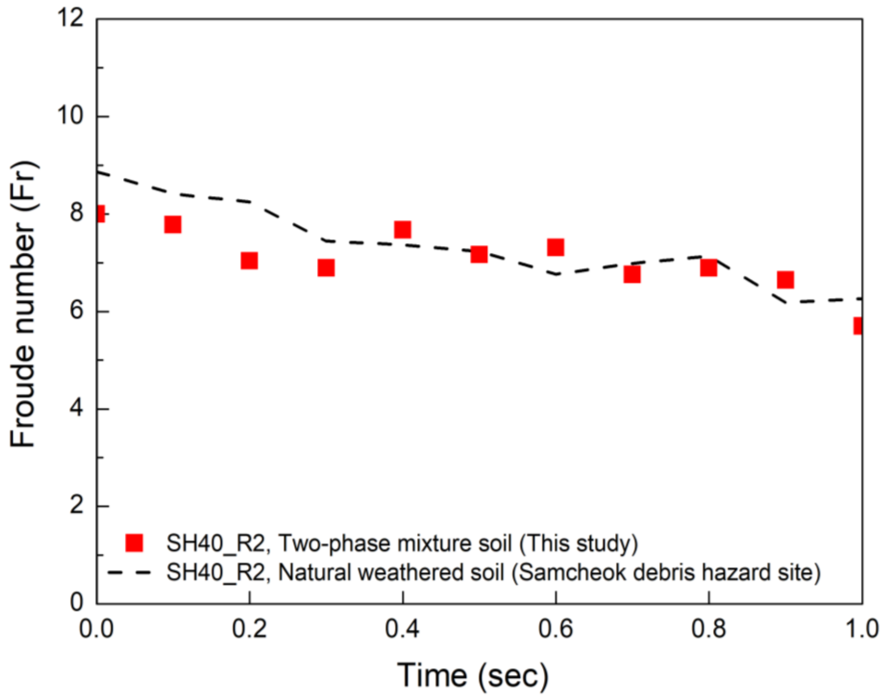

Fig. 10. Comparison of the Froude number for two-phase mixture soil and natural weathered soil.

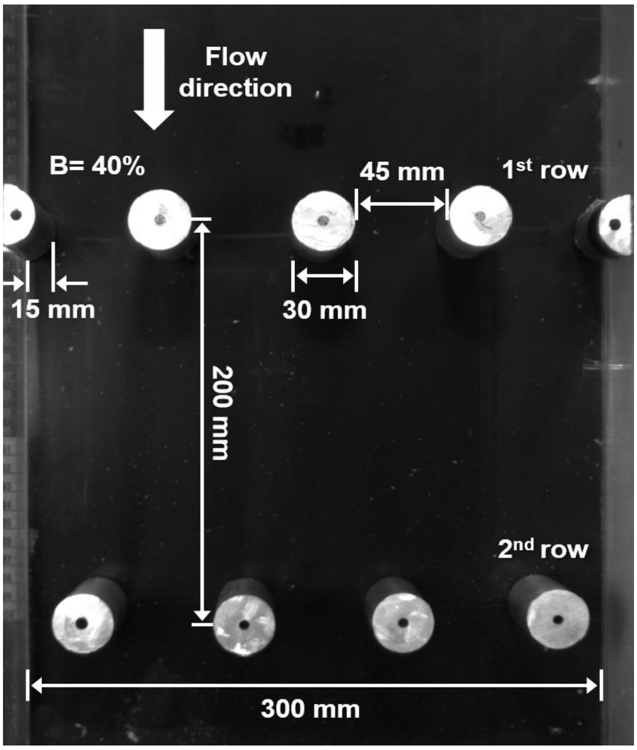

Fig. 11. Installation of a cylindrical baffle array in the small-scale flume (SH60_R2).

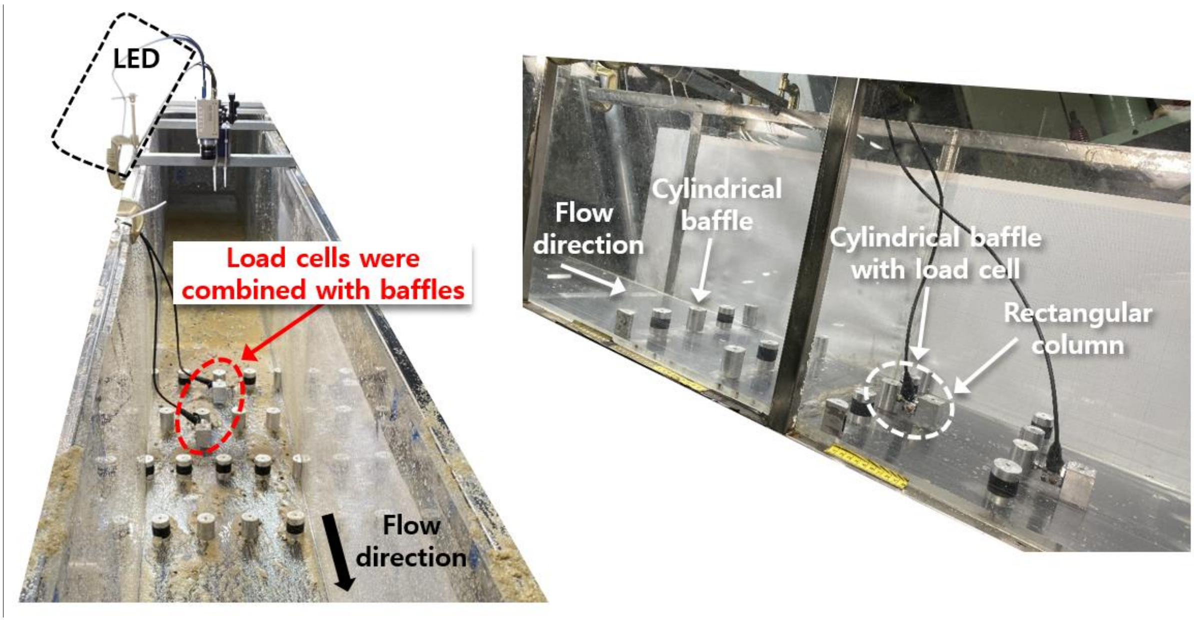

Fig. 12. Installation of a cylindrical baffle array in the small-scale flume (SH40_R4).

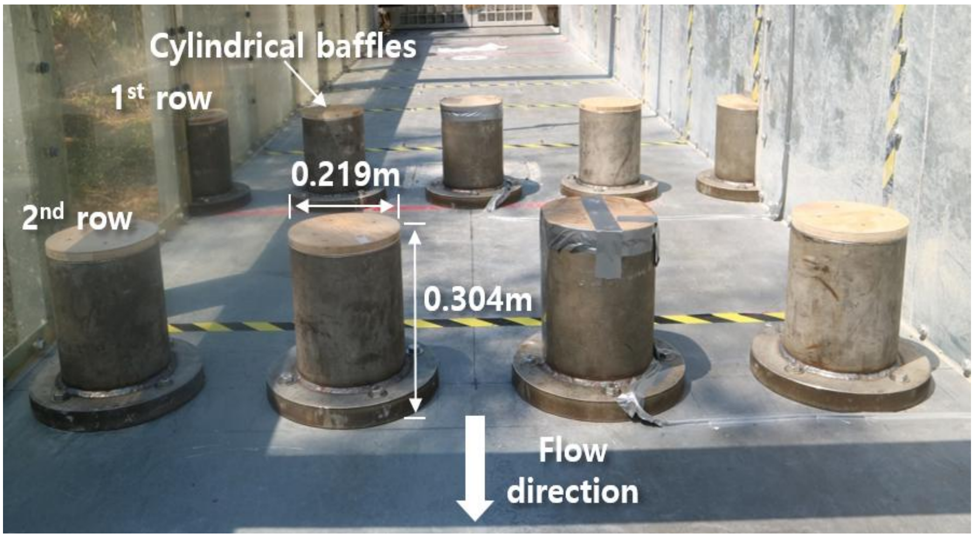

Fig. 13. Installation of a cylindrical baffle array in the large-scale flume (L_R2).

687

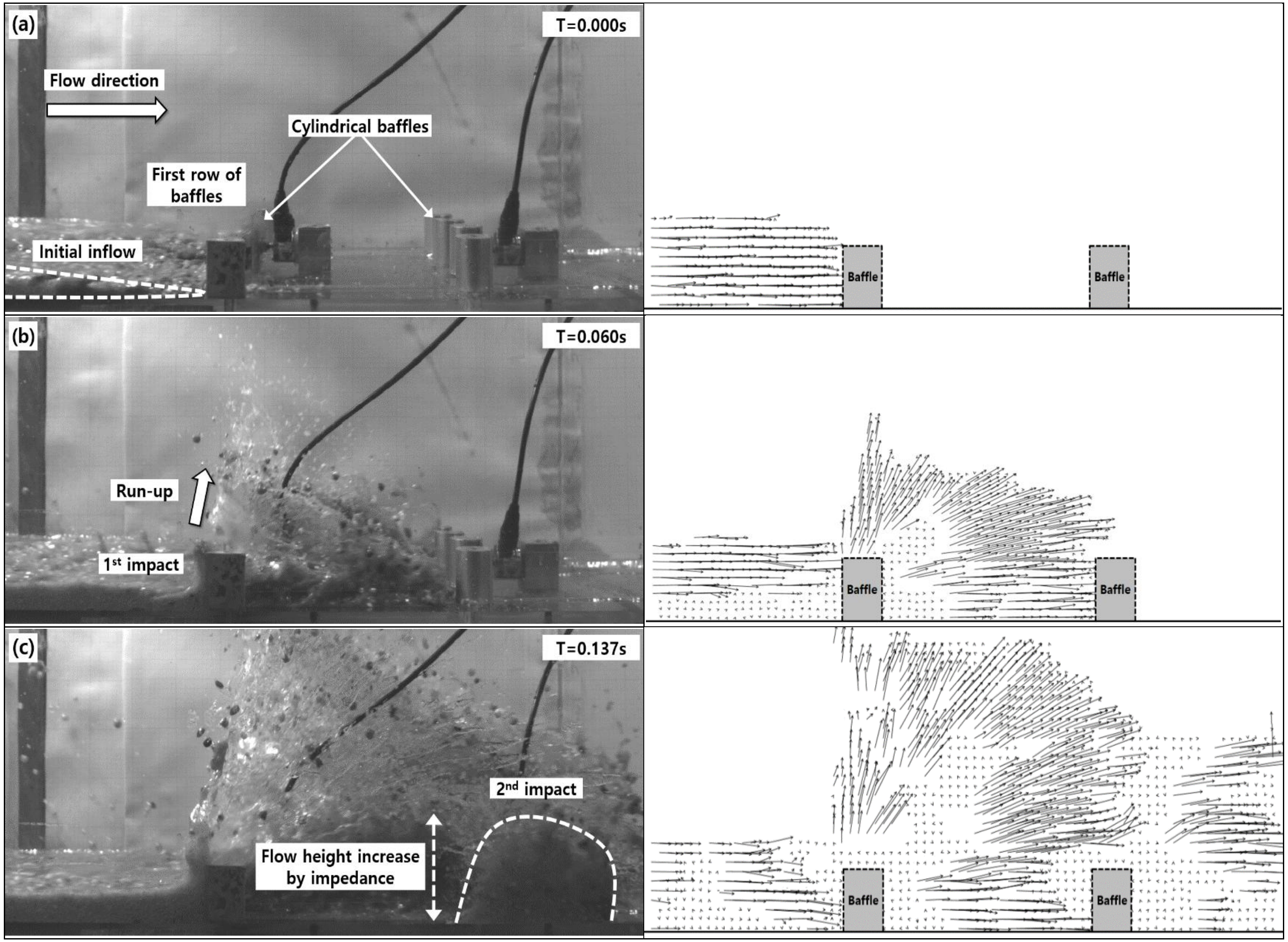

(a)
T=0.000s
Flow direction
Cylindrical baffles
First row of baffles
Initial inflow
Baffle
Baffle
(b)
T=0.060s
Run-up
1st impact
Baffle
Baffle
(c)
T=0.137s
2nd impact
Flow height increase by impedance
Baffle
Baffle

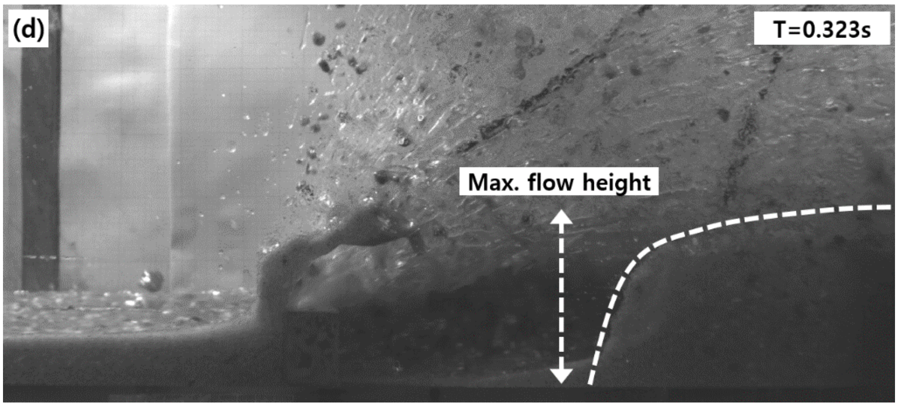

Fig. 14. Side-view flow kinematics of baffle array interaction in small-scale test (SH40_R2).

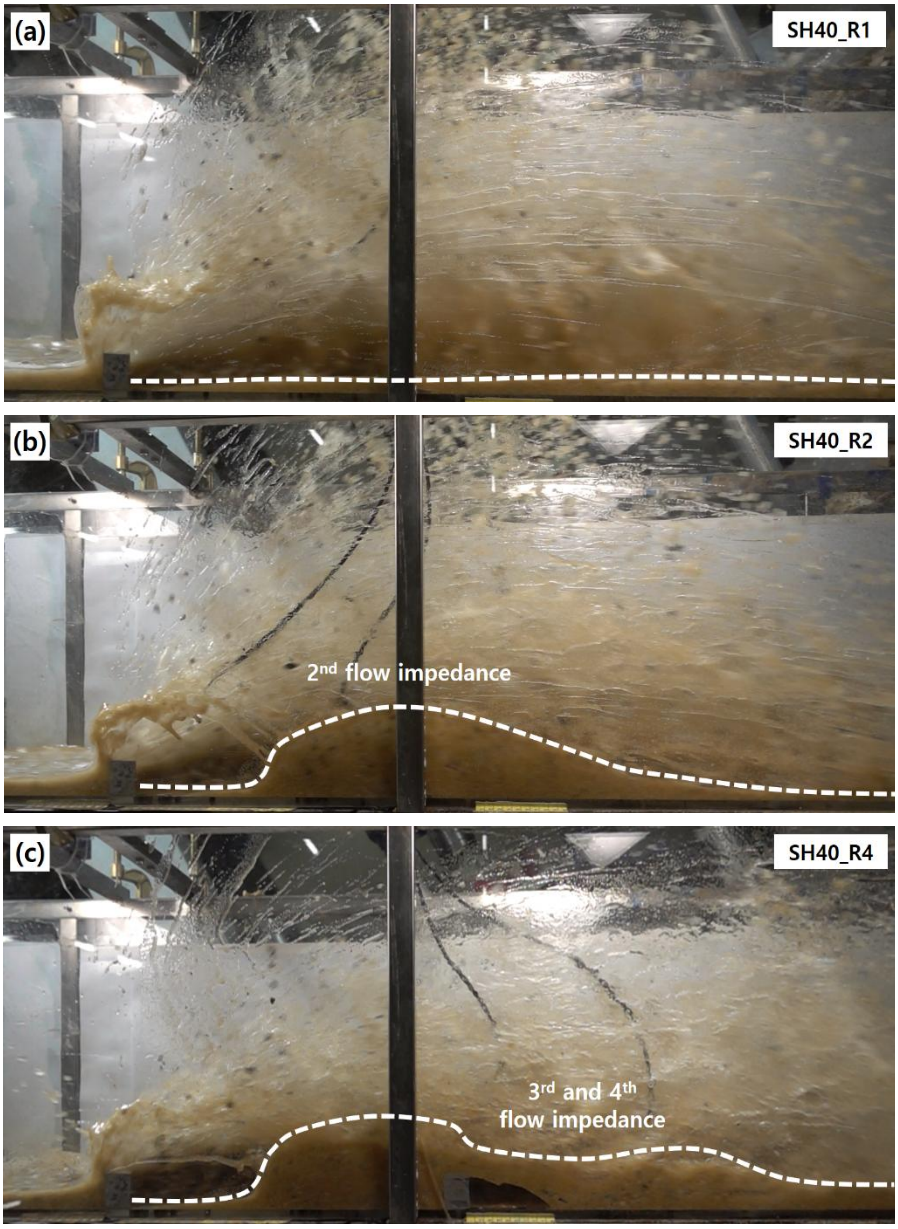

Fig. 15. Effect of baffle array interaction for various numbers of rows in small-scale test: (a) one row (SH40_R1); (b) two rows (SH40_R2); (c) four rows (SH40_R4).

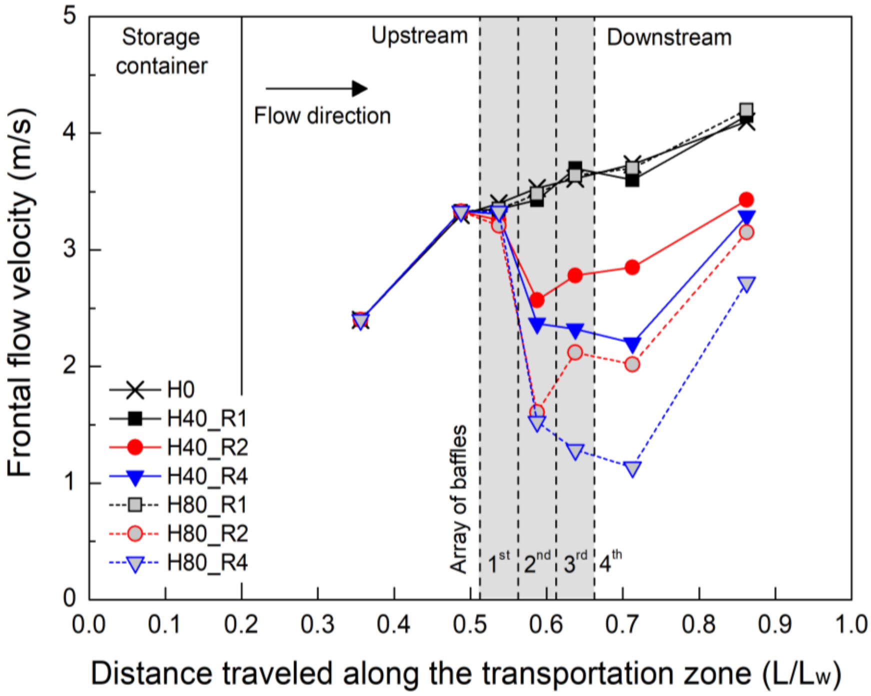

Fig. 16. Frontal velocity along the flume for various baffle configurations.

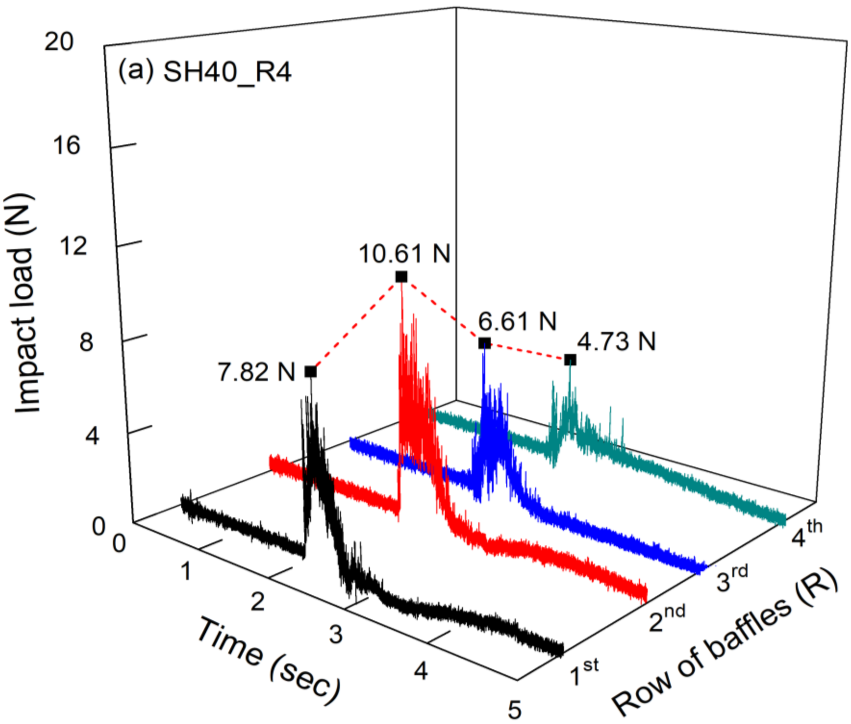

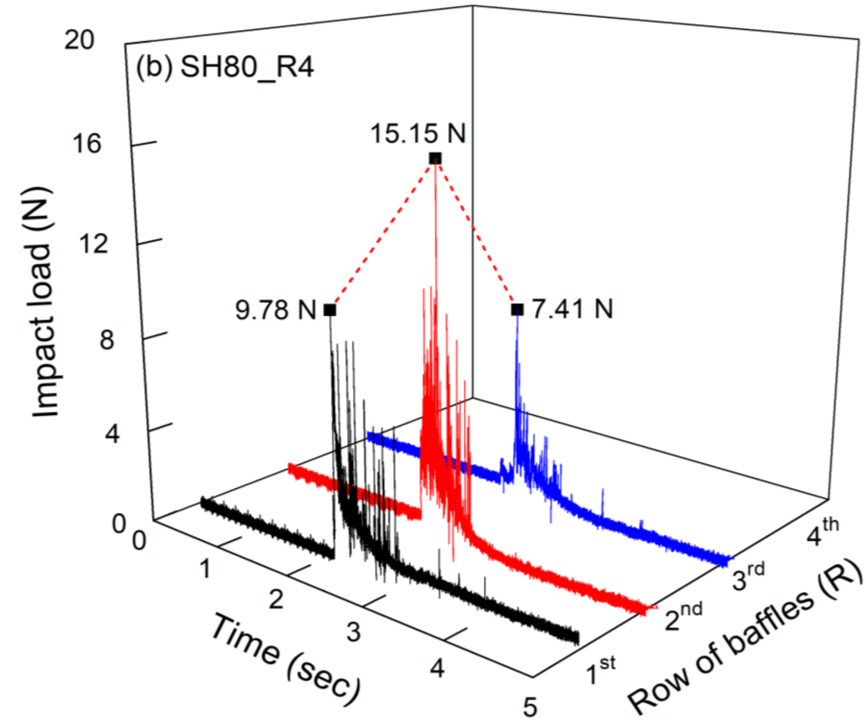

Fig. 17. Impact load with time: (a) 40 mm baffle height (SH40_R4); (b) 80 mm baffle height (SH80_R4).

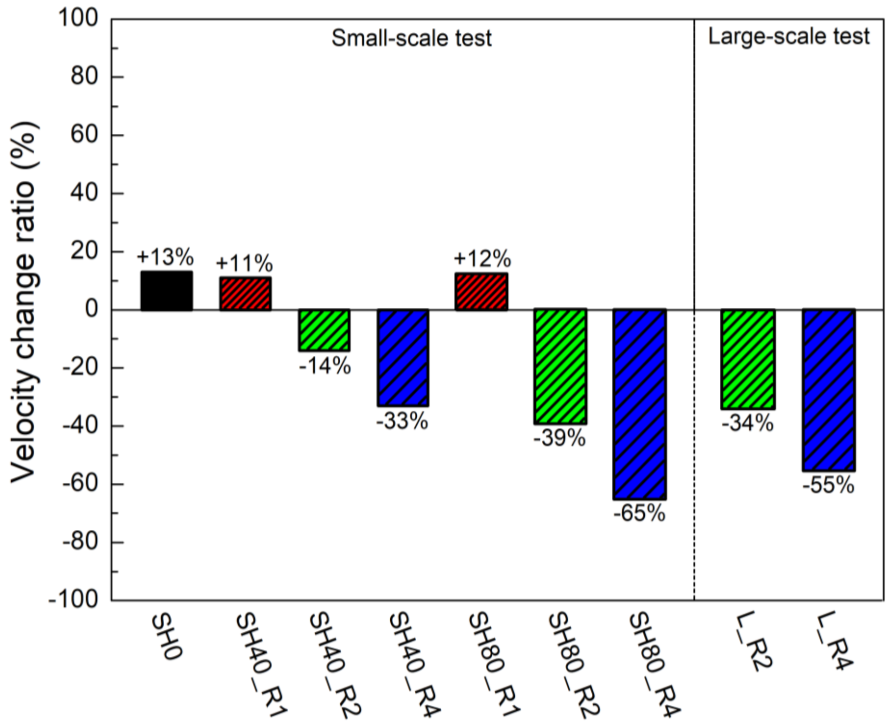

Fig. 18. Velocity reduction for various baffle configurations: (a) small-scale test; (b) large-scale test.

Fig. 19. Side-view flow kinematics of baffle array interaction in large-scale test (L_R2)

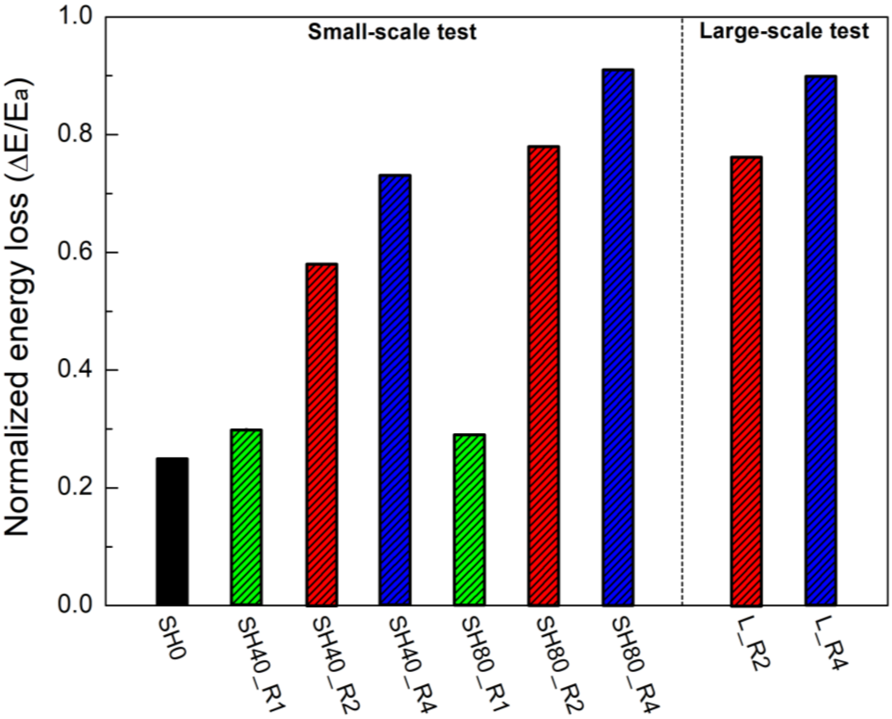

Fig. 20. Normalized frontal flow energy loss: (a) small-scale test; (b) large-scale test.

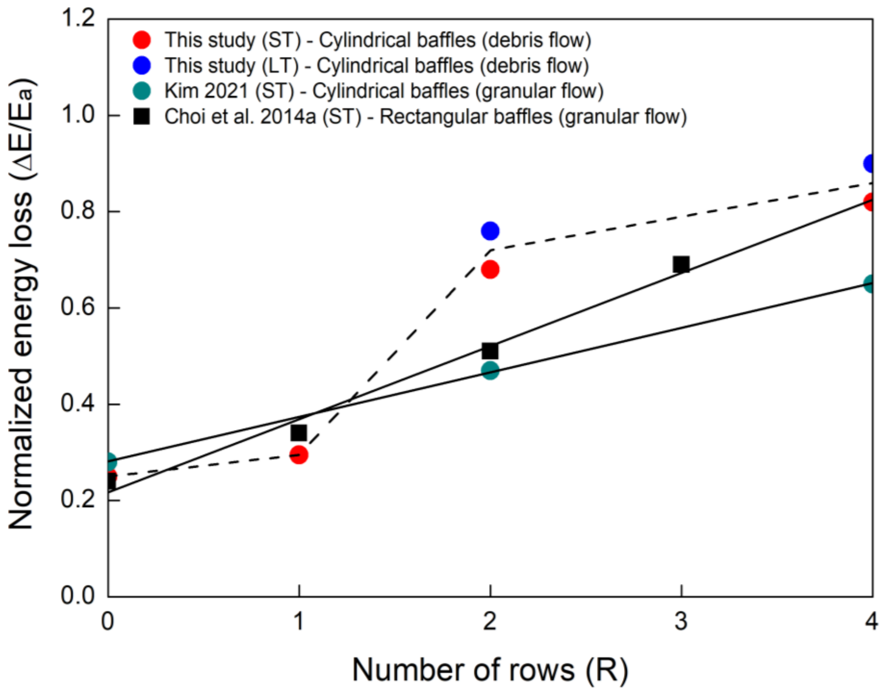

Fig. 21. Normalized energy loss with the number of rows of baffles

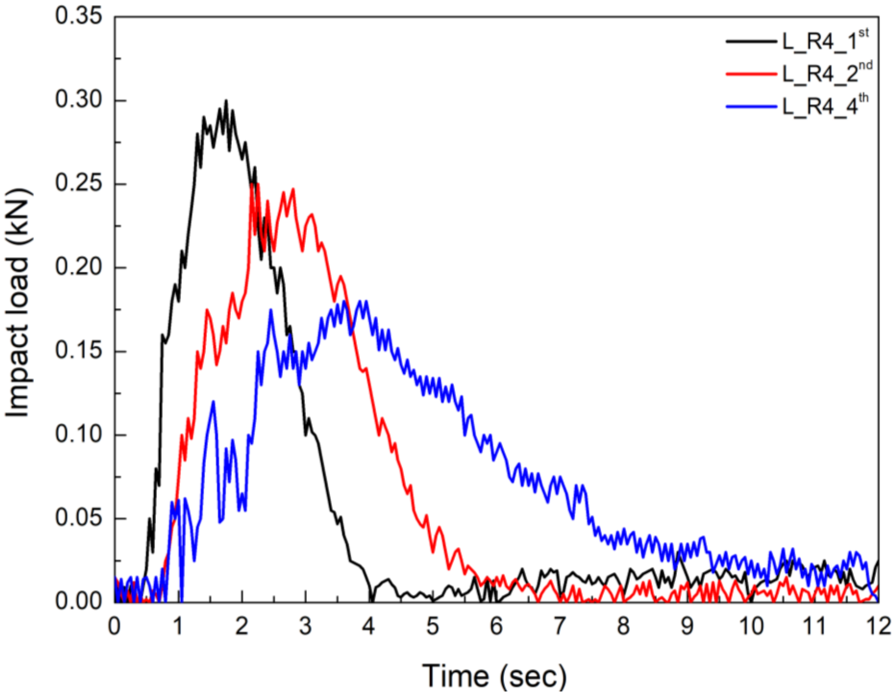

Fig. 22. Impact load with time.

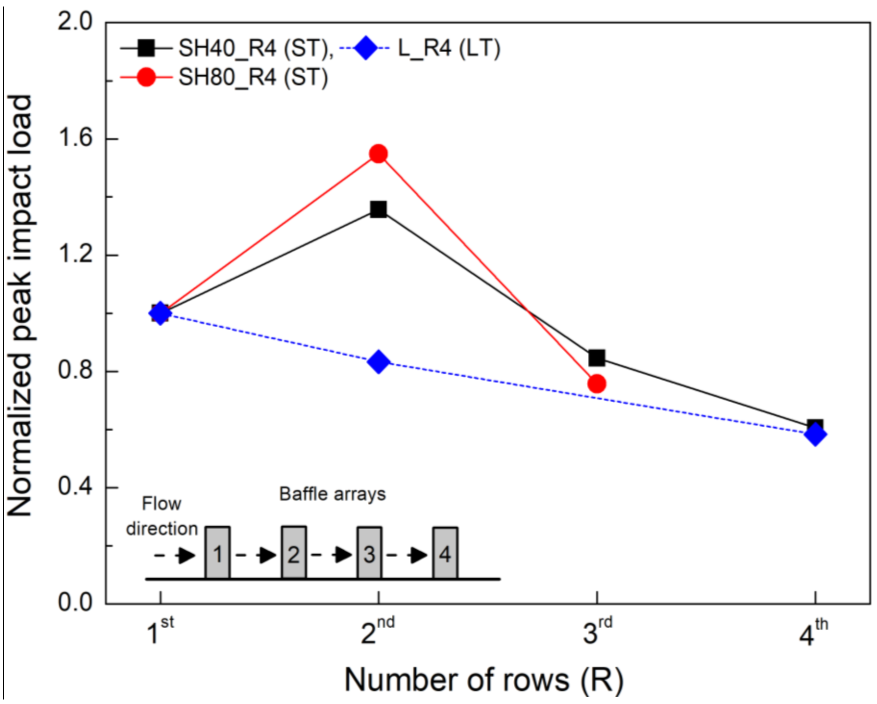

Fig. 23. Variation of peak load in a baffle array.

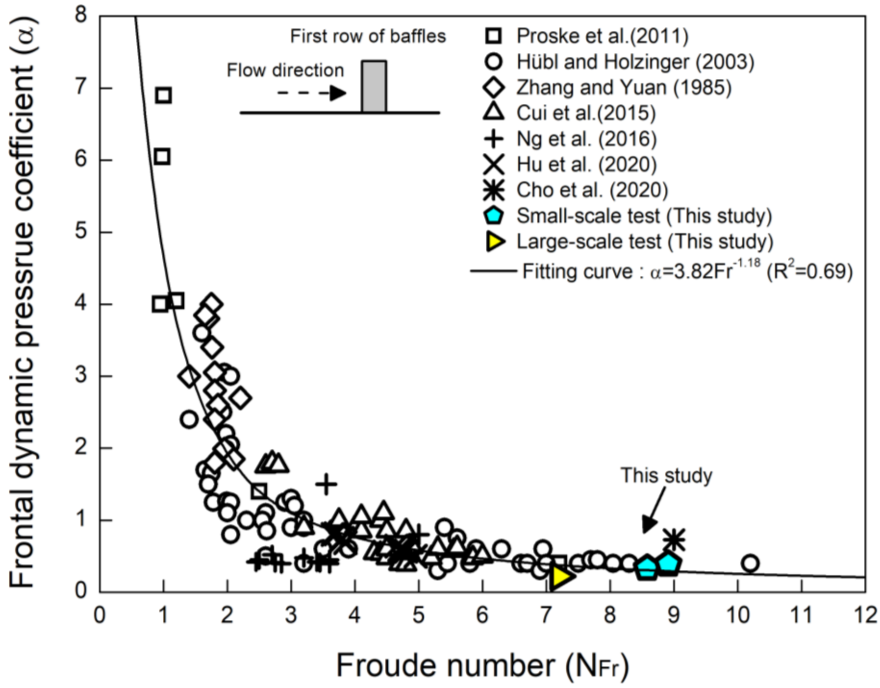

Fig. 24. Relationship between Froude number and empirical coefficients.